ISSN (Print) 1226-1750
ISSN (Online) 2233-6656
Journal of Magnetics 31(1), 39-43 (2026) https://doi.org/10.4283/JMAG.2026.31.1.39

Magnetocrystalline Anisotropy and Magnetostriction in Tetragonally Distorted bcc-Fe and fcc-Ni

Minjae Yoo[1], Bomin Kim[1], Quynh Anh T. Nguyen[1,2], Dorj Odkhuu[3], and S. H. Rhim[1]*

[1]*Department of Physics and Energy Harvest-Storage Research Center, University of Ulsan, Ulsan 44959, Republic of Korea*
[2]*Quantum Magnetic Sensing Group, Korea Research Institute of Standards and Science, Daejeon 34113, Republic of Korea*
[3]*Department of Physics, Incheon National University, Incheon 22012, Republic of Korea*

(Received 2 December 2025, Received in final form 23 January 2026, Accepted 23 January 2026)

Magnetocrystalline anisotropy (MCA) is a preference of direction of magnetization, a fundamental characteristic of magnetic materials. In cubic crystals like bcc-Fe and fcc-Ni, MCA vanishes identically due to symmetry. However, the tetragonal distortion along the z-axis can induce a non-vanishing MCA by breaking the cubic symmetry. Using first-principles calculations, we analyze magnetocrystalline anisotropy energy (E_{MCA}) with respect to c/a ratio, a degree of tetragonalization. For Ni, E_{MCA} is found to be −78 μeV/atom and +89 μeV/atom, while for Fe, it is +44 μeV/atom and −41 μeV/atom at c/a = 1.05 and 0.95, respectively. Based on the analysis of electronic structure, we reveal how band shifts associated with tetragonal distortion drive the MCA. Furthermore, magnetostriction coefficients (λ_{001}) are evaluated, producing values of 23 ppm for Fe and −52 ppm for Ni, consistent with experimental observations.

Keywords : first principles study, magnetocrystalline anisotropy, magnetostriction

1. Introduction

For many decades, magnetism has influenced technological progress, with significant impact by recent research such as spintronics, sensors, and challenging our notion in basic science [1–3]. Among those, key phenomena closely tied to spin-orbit interactions (SOI), such as MCA and Rashba effects have broadened fundamental understanding with innovations in spintronics. More specifically, magnetic random access memory (MRAM) and magneto-optical devices [4–8] have been driving force in spintronics. MCA is a fundamental characteristic of magnetic materials, which is a preference of direction of magnetization. It originates from spin–orbit coupling (SOC) and is highly sensitive to the symmetry of the crystal lattice [9]. This symmetry sensitivity becomes especially important in epitaxial thin films, where lattice mismatch, interfacial strain, and growth conditions imposed by the substrate often distort the film structure and lower the symmetry. Such distortions or lowered symmetry can lead to substantial modifications in MCA, even when the chemical composition remains unchanged [10, 11]. These effects are clearly demonstrated in a number of epitaxial systems. For example, Fe grown on an Ag (001) substrate undergoes a structural transformation from bulk body-centered cubic (bcc) phase to body-centered tetragonal (bct) phase due to epitaxial strain, resulting in significant changes in MCA [12]. Similarly, Ni films deposited on Fe (001) and Au (001) substrates, deviating from the cubic symmetry of bulk Ni, are found with pronounced variations in magnetic anisotropy [13]. In this study, we examine MCA of Fe and Ni by the tetragonalization, demonstrating a transition to perpendicular magnetic anisotropy (PMA) or in-plane magnetic anisotropy (IMA) under compressive or tensile strain. Our analysis based on electronic structure shows that changes in the *c/a* ratio cause substantial MCA variations due to the orbital interactions leading to band shifts, as verified in partial density of states (PDOS) and band structures. Additionally, we also computed magnetostriction coefficients (λ_{001}), showing good agreement with experiments [14, 15].

*Corresponding author: Tel: +82-52-259-2325
Fax: +82-52-259-2646, e-mail: sonny@ulsan.ac.kr

2. Computational methods

We performed density functional theory (DFT) calculations using the Vienna Ab initio Simulation Package (VASP) [16] with the pseudopotential projector augmented wave (PAW) basis [17]. The exchange-correlation potential was treated using the generalized gradient approximation (GGA) proposed by Perdew, Burke, and Ernzerhof (PBE) [18].

Plane-wave energy cutoff was set to 450 eV. For structural optimization, a Γ-centered 21 × 21 × 21 mesh was initially used. Since E_{MCA} is of the order of μeV and highly sensitive to k point sampling, particularly for Fe and Ni due to multi-band contributions near the Fermi level, we carried out an explicit k point convergence test. Based on this test and consistent with Ref. [19], we adopted a denser 22 × 22 × 22-centered mesh for evaluating E_{MCA} for both Fe and Ni to ensure numerical stability. We optimized the lattice parameters a and c while keeping the volume fixed. The energy convergence criterion was set to 10^{-8} eV. MCA is evaluated from the energy difference between two magnetization directions,

$$E_{MCA} = E_{SOC}^{M\|x} - E_{\mathrm{SOC}}^{M\|z} \tag{1}$$

where $\boldsymbol{M}\|x(\boldsymbol{M}\|z)$ denotes the magnetization along the x (z) axis, corresponding to in-plane (out-of-plane) orientation. In our approach, SOC is obtained scalar-relativistically based on the converged ground-state density for each magnetization direction. The SOC interaction is given by

$$E_{SOC} = \frac{\hbar}{2m^2c^2}\frac{1}{r}\frac{dV(r)}{dr}\,\hat{L}\cdot\hat{S} \tag{2}$$

where $V(r)$ is the spherical part of the effective potential inside the PAW sphere, and $\hat{L}$ and $\hat{S}$ are the orbital and spin angular momentum operators, respectively [20].

Fig. 1 shows the crystal structures and corresponding d-orbital energy level of Fe and Ni under tetragonal distortion with (c/a = 0.95, 1.00, and 1.05). In each case, the left side displays the crystal structure, while the right side illustrates the schematic splitting of the d-orbitals. For the cubic structure (c/a = 1.00), the crystal field splits five d-orbitals into two representations, $t_{2g}(d_{xy}, d_{yz}, d_{xz})$ and $e_g(d_{x2-y2}, d_{z2})$. Under tetragonal distortion ($c/a \neq 1$), these levels further split into $a_1(d_{x2-y2})$, $b_1(d_{z2})$, $b_2(d_{xy})$, and $e(d_{xy}, d_{xz})$ representations. The level ordering depends on whether c/a is greater or less than unity, and the splitting depends on the degree of distortion. As Fe and Ni are bcc and fcc, respectively, the level of d states with respect to c/a is opposite, as well known as Jahn–Teller effect of crystal field [21].

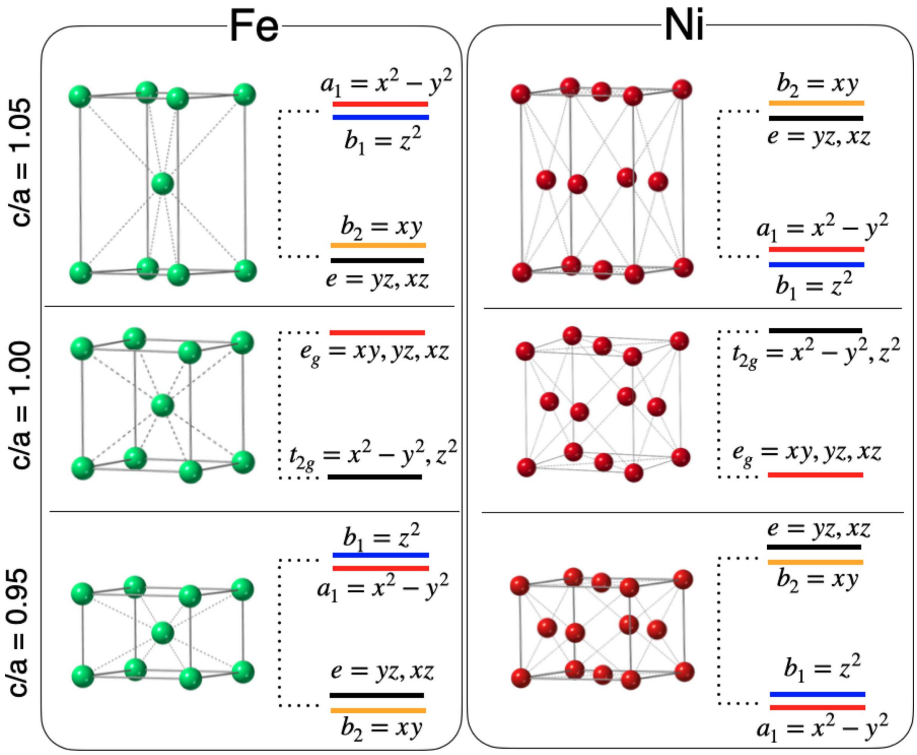

Fig. 1. (Color online) Crystal structure of bcc-Fe (left) and fcc-Ni (right). From top to bottom, c/a = 1.05, 1.00, and 0.95 and corresponding d-orbitals with representations under crystal field.

3. Results and Discussion

3.1. Magnetocrystalline anisotropy

$E_{MCA} > 0$ indicates PMA, while $E_{MCA} < 0$ denotes IMA. In the framework of perturbation theory with the spin-orbit interaction, E_{MCA} is analyzed coupling between occupied and unoccupied states as follows [22]:

$$E_{MCA}^{\sigma\sigma'} \approx \xi^2 \sum_{o,u} \frac{\left|\langle o^{\sigma}|L_z|u^{\sigma'}\rangle\right|^2 - \left|\langle o^{\sigma}|L_x|u^{\sigma'}\rangle\right|^2}{\varepsilon_{u,\sigma'} - \varepsilon_{u,\sigma}}. \quad (3)$$

ξ denotes the strength of SOC; 'o' and 'u' stand for occupied and unoccupied states, respectively, whose corresponding eigenvalues are ε_o and ε_u, respectively. Spin orientations are denoted by σ and σ', either spin-up ($\uparrow$) or spin-down ($\downarrow$).

By this, E_{MCA} is decomposed into spin channel components: spin-conserving $E_{MCA}^{\uparrow\uparrow}, E_{MCA}^{\downarrow\downarrow}$ and spin-flip $E_{MCA}^{\uparrow\downarrow}, E_{MCA}^{\downarrow\uparrow}$ terms. The spin-channel components allow a detailed analysis of contributions from states characterized by different magnetic quantum numbers.

Fig. 2 presents E_{MCA} of Fe and Ni as a function of tetragonal distortion (c/a). For cubic (c/a = 1), E_{MCA} vanishes identically. For c/a < 1, Fe exhibits PMA whereas Ni exhibits IMA. On the other hand, for c/a > 1, the MCA is reversed: Fe shows IMA and Ni shows PMA.

To further understand the feature of E_{MCA}, we focus on the electronic structure with respect to tetragonal distortion. PDOS in Fig. 3 illustrates how d-orbitals change with respect to c/a (0.95, 1.00, and 1.05) for Fe and Ni. For cubic case (c/a = 1.00), as shown in Fig. 3(c) and 3(d), for Fe and Ni, respectively, by the crystal field d-orbitals are split into two-fold and three-fold degenerate states, e_g (d_{z2}, d_{x2-y2}) and t_{2g} (d_{xy}, d_{yz}, d_{xz}). Upon tetragonal distortion ($c/a \neq 1$), the degeneracy is lifted. e_g states split into d_{z2} and d_{x2-y2}; t_{2g} states split into d_{xy} and two-fold (d_{yz}, d_{xz}) states. For Fe, comparing c/a = 1.05 [Fig. 3(a)] and 0.95 [Fig. 3(e)], peaks of d_{z2} and d_{x2-y2} are pronounced near $E_F - 1$ eV (red arrows); those of d_{xy} and (d_{yz}, d_{xz}) are pronounced just above E_F (blue arrows). For Ni, for c/a = 1.05 [Fig. 3(b)] and 0.95 [Fig. 3(f)], PDOS of (d_{yz}, d_{xz}) and d_{xy} orbitals are dominant near E_F (blue arrows), while those of d_{z2} and d_{x2-y2} dominate just above E_F (red arrows). This change of orbitals in PDOS below or above E_F plays an important role in determining the magnetic anisotropy as shown in Fig. 2.

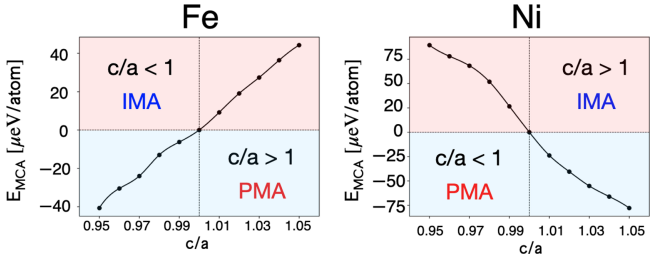

Fig. 2. E_{MCA} as a function of c/a for Fe (left) and Ni (right) for fixed volume. Positive (negative) values correspond to PMA (IMA), as distinguished by the shaded regions.

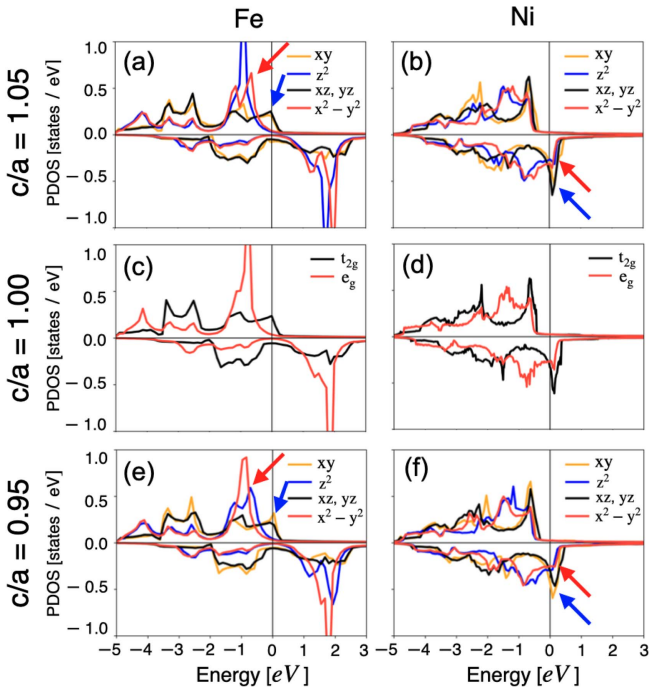

Fig. 3. Spin-polarized partial density of states of d-orbitals for Fe (left) and Ni (right) for c/a ratios of 0.95, 1.00, and 1.05 from bottom to top panel. The upper and lower panels correspond to the spin-majority and spin-minority channels, respectively. For c/a =1.05 and 0.95, d-orbital states are color-coded: d_{z2} in blue, d_{yz} and d_{xz} in black, d_{x2-y2} in red, and d_{xy} in orange. For c/a = 1.00, t_{2g} is in black and e_g in red. Red and blue arrows are marked for c/a=0.95 and 1.05 for discussion of MCA in the text.

To further elucidate the microscopic origin, we analyzed d-orbital contributions in the band structure. Fig. 4 illustrates the band structures of Fe and Ni at c/a ratios of 0.95 and 1.05, presenting the orbital contributions through band thickness. The majority and minority spins are displayed on the left and right panels, respectively.

For Fe, significant band shifts occur as c/a ratio increases from 0.95 to 1.05, particularly at the Γ point, where the minority spin bands play a pivotal role in MCA. As c/a increases, while d_{yz} and d_{xz} bands shift upward relative to E_F, d_{xy} band moves downward, becoming occupied in the minority spin state (blue box in Fig. 4). Simultaneously, d_{x2-y2} and d_{z2} bands switch positions in the unoccupied state (red box in Fig. 4).

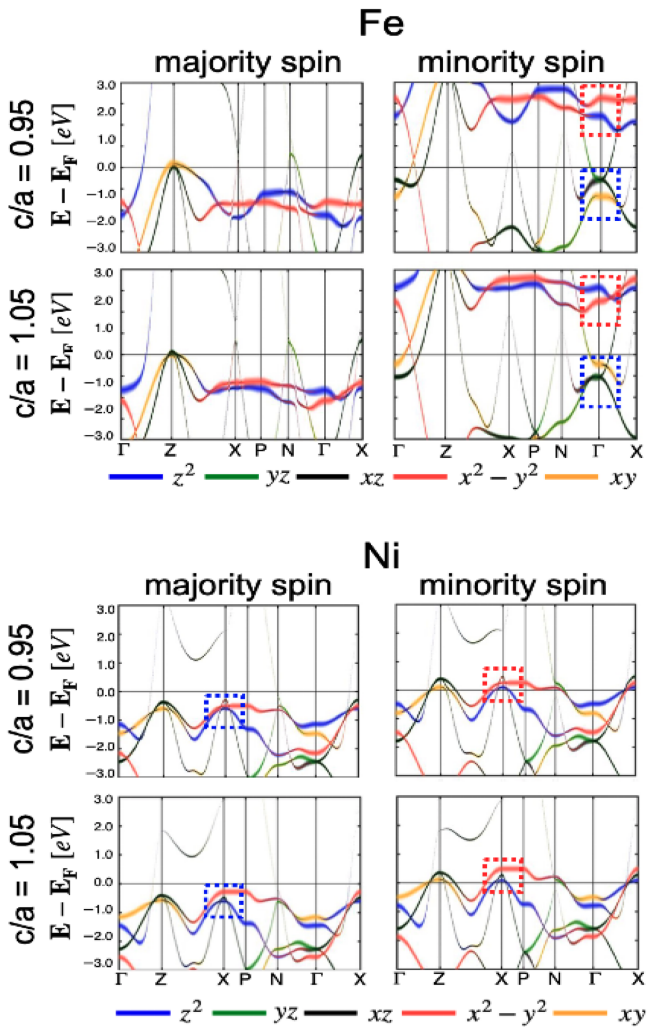

Fig. 4. Spin-resolved band structures of bct Fe (top) and Ni (bottom) at c/a = 0.95 and 1.05. Bands with *d*-orbitals projection: d_{z2} (blue), d_{yz} (green), d_{xz} (black), d_{x2-y2} (red), and d_{xy} (orange). Regions highlighted by red and blue boxes marked for discussion of E_{MCA}.

When c/a = 0.95, the matrix $<d_{yz}, \downarrow |L_x|d_{z2}, \downarrow >$ contributes to IMA, whereas at c/a = 1.05, the matrix $<d_{yz}, \downarrow |L_z|d_{x2-y2}, \downarrow >$ leads to PMA.

For Ni, MCA is primarily influenced by the coupling between the majority and the minority spin states. As c/a increases, d_{x2-y2} band in the majority spin state shifts upward into the unoccupied state, while the d_{yz} and d_{xz} bands move downward (blue box in Fig. 4). Similarly, in the minority spin state, d_{x2-y2} band shifts upward, and the d_{yz} and d_{xz} bands move downward as c/a increases (red box in Fig. 4). When c/a = 0.95, matrices such as $<d_{yz}, \uparrow |L_x|d_{z2}, \downarrow >$ and $<d_{yz}, \uparrow |L_x|d_{x2-y2}, \downarrow >$ yield PMA. Conversely, when c/a = 1.05, matrices like $<d_{yz}, \uparrow |L_x|d_{xz}, \downarrow >$ and $<d_{xz}, \uparrow |L_x|d_{yz}, \downarrow >$ lead to IMA.

Summing up, the orbital-resolved analyses show that tetragonal strain tunes E_{MCA} by reshuffling d-orbital characters near E_F and by switching the dominant SOC channels the minority-spin–conserving processes in Fe versus the interspin spin-flip processes in Ni thereby explaining the sign reversals with c/a (Fig. 2) in line with the PDOS trends (Fig. 3). Because the magnetostriction is governed by the strain derivative of the anisotropy energy, in Sec. 3.2 we determine λ_{001} from the variation of E_{MCA} with c/a for fixed volume.

3.2. Magnetostriction

Magnetostriction refers to the change in the shape or dimensions by change of magnetization. In cubic systems, the strain dependence of magnetization is determined by both the direction of magnetization and the direction of the strain. While the general expression involves directional cosines and multipolar order parameters [23, 24], for the tetragonal distortion along the [001] axis, the relevant magnetostriction coefficient λ_{001} is directly evaluated from energy derivatives,

$$\lambda_{001} = \frac{2}{3}\frac{dE_{MCA}/d(c/c_0)}{d^2E_{tot}/d(c/c_0)^2}, \quad (4)$$

where λ_{001} is expressed as the first derivative of E_{MCA} and the second derivative of the total energy (E_{tot}) with respect to tetragonal strain [25]. Here, c/c_0 represents the degree of tetragonal distortion, and E_{MCA}, as mentioned earlier, is evaluated from the energy difference between in-plane and out-of-plane magnetization at each strain level.

Using Eq. (3), we obtained λ_{001} = +23 ppm for bcc Fe and −52 ppm for fcc Ni. The positive magnetostriction of Fe implies the tensile deformation along the magnetization direction, whereas the negative magnetostriction of Ni does compress along the magnetization. These are in excellent agreement with experiments and previous theoretical calculations as listed in Table 1. Despite the small magnitudes of E_{MCA} and λ_{001}, whose order of magnitudes are μeV and ppm, respectively, signs and trends of magnetostriction confirm the validity of this method for capturing subtle magnetostrictive responses.

The sign and magnitude of λ_{001} can be understood by examining how E_{MCA} varies with tetragonal distortion. In

Table 1. Magnetostriction coefficient (λ_{001}) (in ppm = 10^{-6}) for Fe and Ni.

Atom	Our Result	Theory[a]	EXP[b]
Fe	+23	+29	+21
Ni	−52	−56	−49

[a]Ref. [22] and [b]Ref. [14, 15]

Fe, E_{MCA} increases with increasing c/a, resulting in a positive derivative $dE_{MCA}/d(c/c_0)$, and thus $\lambda_{001} > 0$ corresponding to tensile strain upon magnetization. This behavior can be explained in terms of E_{MCA} by considering the evolution of d-orbitals in the minority-spin upon elongation. As c/a ratio increases, certain unoccupied d-orbitals in the minority-spin channel move closer to the Fermi level. Simultaneously, occupied orbitals shift in a way that increases the orbital overlap, enhancing spin-conserving transitions that contributes to $E_{MCA} > 0$. These orbital shifts are clearly observed in the partial density of states (PDOS) in Fig. 3, particularly around E_F. In contrast, Ni shows a decrease in E_{MCA} with respect to c/a, leading to $\lambda_{001} < 0$, that corresponds to compressive strain along the magnetization. This feature is mainly due to spin-flip transitions between majority-spin occupied states and minority-spin unoccupied states in E_{MCA}. As the structure becomes more elongated, the energy levels and spatial alignment of these orbitals change in a way that reduces the strength of spin–orbit coupling contributions to E_{MCA}. The associated rearrangement of orbital weight near E_F is again evident in PDOS (Fig. 3). As a result, E_{MCA} decreases with strain, giving rise to negative magnetostriction.

4. Conclusions

In this work, we revisit magnetocrystalline anisotropy energy E_{MCA} and tetragonal magnetostriction coefficient (λ_{001}) of bcc Fe and fcc Ni using first-principles density functional theory. Tetragonal distortions were introduced by varying c/a ratio, and the resulting changes in total energy and magnetic anisotropy were systematically analyzed. E_{MCA}, which vanishes in the cubic structure, emerges of order of μeV under distortion-induced symmetry breaking. Using the strain dependence of E_{MCA}, we calculated λ_{001} values of +23 ppm for Fe and −52 ppm for Ni. The results reproduce the correct signs and are in good agreement with experiment and previous theory, demonstrating the effectiveness of this approach for subtle magnetostrictive effects in transition-metal systems.

Acknowledgment

This research is supported by University of Ulsan. We are also grateful for support by the National Supercomputing Center with supercomputing resources (KSC-2025-CRE-0016) and computational resource of the UNIST Supercomputing center.

References

[1] S. A. Wolf, D. D. Awschalom, R. A. Buhrman, J. M. Daughton, S. von Molnar, M. L. Roukes, A. Y. Chtchelkanova, and D. M. Treger, Science **294**, 1488 (2001).
[2] I. Žutić, J. Fabian, and S. D. Sarma, Rev. Mod. Phys. **76**, 323 (2004).
[3] G. Reiss and A. Hütten, Nature Materials **4**, 725 (2005).
[4] I. Karaman, B. Basaran, H. E. Karaca, A. I. Karsilayan, and Y. I. Chumlyakov, Appl. Phys. Lett. **90**, 172505 (2007).
[5] A. Hirohata, K. Yamada, Y. Nakatani, I.-L. Prejbeanu, B. Diény, P. Pirro, and B. Hillebrands, J. Magn. Magn. Mater. **509**, 166711 (2020).
[6] B. Tudu and A. Tiwari, Vacuum **146**, 329 (2017).
[7] D. Apalkov, A. Khvalkovskiy, S. Watts, V. Nikitin, X. Tang, D. Lottis, K. Moon, X. Luo, E. Chen, A. Ong, *et al.*, ACM Journal on Emerging Technologies in Computing Systems (JETC) **9**, 1 (2013).
[8] B. Koopmans, M. Van Kampen, J. T. Kohlhepp, and W. J. M. De Jonge, Phys. Rev. Lett. **85**, 844 (2000).
[9] R. Wu and A. J. Freeman, J. Magn. Magn. Mater. **200**, 498 (1999).
[10] H. Wang, C. Du, P. C. Hammel, and F. Yang, Physical Review B **89**, 134404 (2014).
[11] J. A. Heuver, A. Scaramucci, Y. Blickenstorfer, S. Matzen, N. A. Spaldin, C. Ederer, and B. Noheda, Phys. Rev. B **92**, 214429 (2015).
[12] W. Egelhoff Jr, I. Jacob, J. Rudd, J. Cochran, and B. Heinrich, J. Vac. Sci. Technol. A: Vacuum, Surfaces, and Films **8**, 1582 (1990).
[13] Y. Kamada and M. Matsui, J. Phys. Soc. Jpn. **66**, 658 (1997).
[14] E. W. Lee, Rep. Prog. Phys. **18**, 184 (1955).
[15] D. I. Bower, Proc. R. Soc. Lond. A. Math. Phys. Sci. **326**, 87 (1971).
[16] G. Kresse and J. Furthmüller, Phys. Rev. B **54**, 11169 (1996).
[17] G. Kresse and D. Joubert, Phys. Rev. B **59**, 1758 (1999).
[18] J. P. Perdew, K. Burke, and M. Ernzerhof, Phys. Rev. Lett. **77**, 3865 (1996).
[19] T. Burkert, O. Eriksson, P. James, S. I. Simak, B. Johansson, and L. Nordström, Phys. Rev. B **69**, 104425 (2004).
[20] D. Odkhuu, Sci. Rep. **8**, 6900 (2018).
[21] D. Odkhuu, S. H. Rhim, N. Park, K. Nakamura, and S. C. Hong, Phys. Rev. B **91**, 014437 (2015).
[22] D.-S. Wang, R. Wu, and A. J. Freeman, Phys. Rev. B **47**, 14932 (1993).
[23] R. Wu, L. J. Chen, A. Shick, and A. J. Freeman, J. Magn. Magn. Mater. **177**, 116 (1998).
[24] A. J. Freeman, R. Wu, M. Kim, and V. Gavrilenko, J. Magn. Magn. Mater. **203**, 1 (1999).
[25] D. Odkhuu, W. S. Yun, S. H. Rhim, and S. C. Hong, Appl. Phys. Lett. **98**, 152502 (2011).